

Probing vacuum birefringence by phase-contrast Fourier imaging under fields of high-intensity lasers

K. Homma^{1,2}, D. Habs² and T. Tajima²

¹ Graduate School of Science, Hiroshima University, Kagamiyama, Higashi-Hiroshima 739-8526, Japan

² Fakultät für Physik, Ludwig-Maximilians Universität München, D-85748 Garching, Germany

Received: date / Revised version: date

Abstract In vacuum high-intensity lasers can cause photon-photon interaction via the process of virtual vacuum polarization which may be measured by the phase velocity shift of photons across intense fields. In the optical frequency domain, the photon-photon interaction is polarization-mediated described by the Euler-Heisenberg effective action. This theory predicts the vacuum birefringence or polarization dependence of the phase velocity shift arising from nonlinear properties in quantum electrodynamics (QED). We suggest a method to measure the vacuum birefringence under intense optical laser fields based on the absolute phase velocity shift by phase-contrast Fourier imaging. The method may serve for observing effects even beyond the QED vacuum polarization.

1 Introduction

To observe nonlinear responses of matter, the pump-probe technique is widely used: Matter is first excited by an intense laser pulse and then probed by a delayed weaker laser pulse. When the vacuum is considered as a part of matter, the most natural approach to probe it is, hence, the pump-probe technique. Maxwell's equations in vacuum, however, allow only for linear superpositions of laser fields. In quantum mechanics, a photon can be resolved into a pair of virtual fermions over a short time via the uncertainty principle in the higher frequency domain even below the fermion mass scale. The loop of the virtual pair provides a coupling to photons, resulting in a photon-photon interaction. In the optical frequency domain, the electron-positron loop and possibly the lightest quark-antiquark loop are expected to give rise to the photon-photon interaction with the mass scale of the electron being $0.5 \text{ MeV}/c^2$ and of the lightest

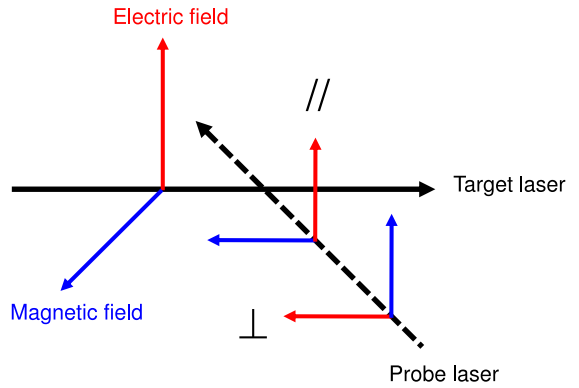


Fig. 1 Polarization directions of the target and probe lasers.

quark ranging from $\sim 1 - 100 \text{ MeV}/c^2$, respectively. Below the electron mass scale, there is no known mass scale relevant for photon-photon interactions in the standard model of particle physics. In this paper we focus on the photon-photon interaction in the optical laser frequency range based on quantum electrodynamics (QED).

In the low-frequency collision $\hbar\omega \ll m_e c^2$, it is sufficient to describe the photon-photon interaction by the effective one-loop Lagrangian [1, 2, 3]

$$L_{1-loop} = \frac{1}{360} \frac{\alpha^2}{m_e^4} [4(F_{\mu\nu} F^{\mu\nu})^2 + 7(F_{\mu\nu} \tilde{F}^{\mu\nu})^2], \quad (1)$$

where $\alpha = \frac{e^2}{\hbar c}$ is the fine structure constant, m_e is the electron mass, $F_{\mu\nu} = \partial A_\mu / \partial x^\nu - \partial A_\nu / \partial x^\mu$ is the antisymmetric field strength tensor and its dual tensor $\tilde{F}^{\mu\nu} = 1/2 \epsilon^{\mu\nu\rho\sigma} F_{\rho\sigma}$ with the Levi-Civita symbol $\epsilon^{\mu\nu\rho\sigma}$.

Based on this Lagrangian, the dispersion relation for photons in vacuum is expected to be modified by intense electromagnetic fields. This effect under a constant electromagnetic field was first discussed by Toll [4]. At optical frequencies, we may approximate the time-varying

electromagnetic field as a constant field, because the relevant time scale for the creation of virtual electron-positron pairs is much shorter than that of the inverse of optical frequencies. We can discuss the dispersion relation and the birefringent nature via measurements of the refractive index, *i.e.*, the inverse of the phase velocity as illustrated in Fig.1, where a linearly polarized probe laser beam crosses a linearly polarized target laser beam. The measurements of the phase velocity shift when the electric fields of both lasers are either parallel or normal to each other are specified with subscripts \parallel or \perp , respectively. The theoretical derivation of these quantities in the linearly polarized electromagnetic field of the target (the so-called crossed-field configuration, where the electric field \hat{E} and magnetic field \hat{B} are normal at the same strength) was originally studied in [5,6] and further derived from the generalized prescription based on the polarization tensor, applicable to arbitrary external fields, in [7]. This results in

$$\begin{aligned} v_{\parallel}/c &= 1 - \frac{8}{45} \alpha^2 \frac{\rho_t}{\rho_c}, \\ v_{\perp}/c &= 1 - \frac{14}{45} \alpha^2 \frac{\rho_t}{\rho_c}, \end{aligned} \quad (2)$$

where v_{\parallel}/c and v_{\perp}/c are the phase velocities when the combination of linear polarizations of the probe and target lasers is parallel and normal, respectively. The quantity $\rho_c \equiv m_e^4 c^5 / \hbar^3 \sim 1.42 \times 10^6 \text{ J}/\mu\text{m}^3$ is the Compton energy density of an electron and ρ_t is defined as z_k/k^2 where k is the wave number of the probe electromagnetic field with the unit vector of \hat{k} . The Lorentz-invariant quantity z_k is defined as

$$z_k = (k_{\alpha} F^{\alpha\kappa})(k_{\beta} F^{\beta}_{\kappa}), \quad (3)$$

and the relation to the energy density ϵ^2 in the crossed field condition is

$$\frac{z_k}{k^2} = \epsilon^2 (1 + (\hat{k} \cdot \hat{n}))^2, \quad (4)$$

with $\epsilon = E = cB$ and $\hat{n} = \hat{B} \times \hat{E}$ with $\hat{\cdot}$ indicating the unit vector. Thus the second terms in Eq. (2) show that the deviation of the phase velocities of light v_{\parallel} and v_{\perp} are proportional to the field energy density normalized to the Compton energy density of an electron. The shift of the refractive index from that of the normal vacuum is on the order of 10^{-11} for the energy density ϵ^2 of $1 \text{ J}/\mu\text{m}^3$ corresponding to the power density of a high-power laser beam focused to $10^{22} \text{ W}/\text{cm}^2$ at its waist. The refractive medium exhibits a polarization dependence, *i.e.*, it shows birefringence. The difference in v_{\parallel} and v_{\perp} in Eq. (2) results from the first and second terms in the bracket of the effective one-loop Lagrangian in Eq. (1).

The dispersion relation and the birefringence under a constant electromagnetic field in the UV limit ($\omega \rightarrow \infty$) may be evaluated via the Kramers-Kronig dispersion relation, as discussed in [8]. The phase velocity in both UV

and IR is expected to be subluminal ($v_{phase} < c$) under the influence of the QED field [8,7]. The UV limit of the phase velocity is supposed to govern causality which should not exceed the velocity of light in vacuum. Therefore, it can be a fundamental test of a variety of effective field theories in the IR by testing whether the phase velocity in the UV limit, extrapolated from that of the IR, is superluminal ($v_{phase}(\infty) > c$) or not. Thus far the dispersion relation from IR to UV is theoretically known only in the QED field [8]. However, there is no data so far even in the domain of IR frequencies. It is important, therefore, for experiments to quantitatively verify or disprove the QED prediction. We note that the measurement of the refractive index in the domain of higher frequencies may be sensitive to the part of the anomalous dispersion where the real part of the refractive index rises as discussed in [9], and, also, the measurement of the electron-positron pair creation [10,11,12,13] in strong electromagnetic fields may be directly sensitive to the absorptive or imaginary part. The Kramers-Kronig relation connects the real and imaginary parts of the forward scattering amplitude or the refractive index. Therefore, the systematic measurements of real and imaginary parts over a wide frequency range may provide a test ground of QED and the Kramers-Kronig relation itself, when it is applied to the vacuum.

The key issue is how to detect the extremely small refractive index change, resulting from the photon-photon interaction between the target and probe lasers. The conventional way in the X-ray frequency range is based on a measurement of the ellipticity caused by the target field-induced birefringence with respect to the linearly polarized incident probe photons [9,23]. Since nowadays high-precision X-ray polarimetry technique is available [14], we may reach the sensitivity to QED-induced birefringence, if high-intensity lasers such as those attainable in ELI [15] are provided. As explained above, the probe frequency dependence of the birefringence is important to complete the QED-induced dispersion relation. Therefore, we need measurements in the optical frequency range as well. The conventional ways in the range of optical frequencies that were performed [21] and proposed [22] are again based on a measurement of the ellipsoid caused by the birefringence and a measurement of the rotation angle of a linearly polarized probe laser by making it propagate for a long distance under the influence of a weak magnetic [21] or electromagnetic field [22]. This method has the advantage to enhance the phase shift by a long optical path without introducing costly strong target electromagnetic fields. In the case of a constant magnetic field on the order of 1 T, one encounters the limits of physical sensitivity to the QED nonlinear effects. In the case of an electromagnetic field, we may be sensitive to the QED-induced birefringence within a few days with a 1J CW laser according to the claim in [22]. However, if one aims at the sensitivity even beyond QED-induced birefringence as we discuss in section 3,

it is essential to introduce a high-intensity pulse even beyond the capability of the ELI facility [15]. In such circumstances the storage of a high-intensity laser pulse in a cavity is limited by the damage threshold of the optical elements needed to store the target field over a long time.

On the other hand, if we could localize the field-induced refractive index change by tightly focusing a high-intensity target laser pulse and measuring the spatially inhomogeneous phase effect of the vacuum on a pulse-by-pulse basis, there will be no physical limit in increasing the intensity of the laser pulse until the vacuum itself breaks down. In order to increase the shift of the refractive index, corresponding to the inverse of the phase velocities in Eq. (2), *i.e.*, the intensity of the target laser pulse as expected from Eq. (3) and Eq. (4), it is necessary to use a focused laser pulse by confining the large laser energy into a small space-time volume. This causes a locally varying refractive index along the trajectory of the target laser pulse in vacuum. A variation of the refractive index arises over the high-intensity part and the remaining vacuum. If the probe laser penetrates into both parts simultaneously, the corresponding phase contrast should be embedded in the transverse profile of the same probe laser. Our suggestion is to directly measure the phase contrast and to determine the absolute value of the refractive index change by controlling the combination of polarizations of the probe and target laser pulses. This should result in the birefringence as expected in Eq. (2). The birefringence measurement based on the measurement of absolute phase velocities we suggest here should be contrasted to any existing techniques to measure the ellipticity where only relative phase differences can be discussed.

In the following sections we introduce the basic concept of the phase-contrast Fourier imaging by crossing target and probe lasers and discuss a way to extract a physically induced phase in the presence of a phase background. We then discuss also other physical contributions beyond QED, to which this imaging method may be applied.

2 Phase-contrast Fourier imaging

We now consider an experimental setup, where we create a high-intensity spot by focusing a laser pulse in vacuum and probe its refractive index shift by a second laser pulse. We call the first laser pulse the target laser pulse, while from hereon the second laser pulse will be denoted as the probe laser pulse. We need to detect the extremely small shift of the phase velocity by the target-probe interaction. For this we also need an intense probe laser in order to enhance the visibility. However, if we utilize conventional interferometer techniques, providing a homogeneous phase contrast over the probe laser profile, such small refractive index changes are hard to detect.

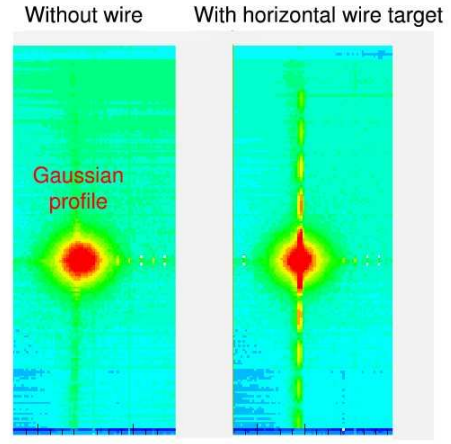


Fig. 2 Far-field diffraction patterns from a thin-wire target, when a Gaussian laser pulse is shot onto the wire. The left figure describes the situation without wire. The right figure shows the case when the thin-wire target is horizontally arranged.

This is because the resulting intensity modulation always appears on top of a huge pedestal intensity, with an extremely small contrast between the modulation and the pedestal. Any photo-detection device will not be sensitive to the small number of photons spatially distributed over the pedestal intensity beyond 1 J ($\sim 10^{18}$ visible photons), due to the limited dynamic range of the photon intensity measurable by a camera pixel without causing saturation of the intensity measurement. On the other hand, broadening the dynamic range by lowering the gain of the electric amplification of photo-electrons degrades the sensitivity to the small number of the spatially distributed photons or the sensitivity to the small phase shift. Therefore, we need to invent a method that can spatially separate the weakly modulated characteristic intensity pattern from the strong pedestal.

In order to overcome this difficulty, we suggest utilizing the inhomogeneous phase-contrast Fourier imaging in the focal plane by focusing the probe laser. The physically embedded phase contrast on the transverse profile of the probe laser amplitude is Fourier transformed onto the focal plane due to the effect of the added phase by the lens. Actually, a parabolic mirror is necessary to avoid dispersion and damage by high-intensity irradiation. This will be considered later. The intensity pattern in the focal plane exhibits the preferable feature, that the characteristic phase boundary causes outer regions of the intensity profile far from the focal point to expand, whereas a Gaussian laser beam with a homogeneous phase converges into a small focal spot at its waist. It is instructive to illustrate the characteristic nature of the diffraction pattern from a wire-like target as shown in Fig. 2. Here the far-field pattern, known as Fraunhofer diffraction, is shown in the case when a Gaussian laser beam irradiates a thin-wire target. This

can be understood as the Fourier transform of the wire shape, approximated as a rectangle of $2\mu \times 2\nu$. It is well known that a lens produces a far-field diffraction pattern, corresponding to the exact Fourier-transformed image of the object in the front focal plane (e.g. see [25, 27]). In order to understand the diffraction image, we may qualitatively refer to Babinet's principle, which states that the diffraction pattern from an opaque wire plus that of a slit of the same size and shape form an amplitude distribution identical to that of the incident wave. Therefore, the characteristic diffraction patterns from the wire and the slit are similar, but deviate from each other such that they interfere to reconstruct the incident wave. The intensity pattern after Fourier transform of such a rectangular slit is expressed as

$$\left(\frac{\sin(\mu\omega_x)}{\mu\omega_x}\right)^2 \left(\frac{\sin(\nu\omega_y)}{\nu\omega_y}\right)^2, \quad (5)$$

where $\omega_x = \frac{2\pi}{\lambda f}x$ and $\omega_y = \frac{2\pi}{\lambda f}y$ are the spatial frequencies for the given position (x, y) in the focal plane of the lens/mirror with the focal length f at the wavelength λ , respectively. In the case of a slit with $\mu \gg \nu$, the rectangular profile in the focal plane emerges as a pattern of dark and bright fringes perpendicular to the slit (see Fig. 2 (right)). The narrower the slit size is, the further the fringes move apart. On the other hand, a Gaussian beam without wire or slit remains unchanged, because the Fourier transform of a Gaussian beam remains a Gaussian beam (see Fig. 2 (left)). This is the key feature that drastically improves the detectability of small phase shifts by sampling only outer parts of the diffraction pattern. This may also be interpreted as the counter-concept to the conventional spatial filter, where outer parts are eliminated to maintain a smooth phase on the transverse profile of the Gaussian distribution.

Given the intuitive picture above, a quantitative formulation of our proposed method is presented as follows. In order to discuss the amount of the phase shift, we need a distinct geometry of both the target and probe lasers. Let us first consider the laser profile assuming Gaussian beams. The solution of the electromagnetic field propagation along z in vacuum is well-known [27]. The electric field component corresponding to the transverse mode l, m and *e.g.* polarized along y is expressed as $\mathbf{E}(x, y, z, t) = \text{Re}\{\mathbf{e}_y \psi_{l,m}(x, y, z) e^{i\omega t}\}$ with

$$\psi_{l,m}(x, y, z) = A_0 \frac{w_0}{w(z)} H_l \left(\frac{\sqrt{2}}{w(z)} x \right) H_m \left(\frac{\sqrt{2}}{w(z)} y \right) \times \exp \left\{ -i[kz - (l + m + 1)\eta(z)] - r^2 \left(\frac{1}{w(z)^2} + \frac{ik}{2R(z)} \right) \right\} \quad (6)$$

where the H_l are l -th order Hermite polynomials, $k = 2\pi/\lambda$, $r = \sqrt{x^2 + y^2}$, w_0 is the waist, which cannot be smaller than λ due to the diffraction limit, and other

definitions are as follows:

$$w(z)^2 = w_0^2 \left(1 + \frac{z^2}{z_R^2} \right), \quad (7)$$

$$R = z \left(1 + \frac{z_R^2}{z^2} \right), \quad (8)$$

$$\eta(z) = \tan^{-1} \left(\frac{z}{z_R} \right), \quad (9)$$

$$z_R \equiv \frac{\pi w_0^2}{\lambda}. \quad (10)$$

In order to determine the normalization factor A_0 , we use the orthonormal condition of the n^{th} Hermite polynomial as follows

$$\int_{-\infty}^{+\infty} H_n(\xi)^2 e^{-\xi^2} d\xi = 2^n n! \sqrt{\pi}. \quad (11)$$

With the replacement $\xi = \frac{\sqrt{2}}{w_0} x$ we obtain

$$\int_{-\infty}^{+\infty} H_l^2 \left(\frac{\sqrt{2}}{w_0} x \right) e^{-\frac{2x^2}{w_0^2}} dx \int_{-\infty}^{+\infty} H_m^2 \left(\frac{\sqrt{2}}{w_0} y \right) e^{-\frac{2y^2}{w_0^2}} dy = \frac{1}{2} w_0^2 \pi 2^{l+m} l! m! \quad (12)$$

At $z = 0$ we can then relate the amplitude A_0 with the beam power P_0 by

$$P_0 = A_0^2 \int_{-\infty}^{+\infty} \int_{-\infty}^{+\infty} \psi_{l,m}(x, y) \psi_{l,m}^*(x, y) dx dy \quad (13)$$

yielding

$$A_0^2 \equiv \frac{P_0}{2\pi\sigma^2 2^{l+m} l! m!}, \quad (14)$$

where w_0 is replaced by 2σ and A_0^2 is the on-axis intensity at the waist.

Figure 3 illustrates the conceptual experimental setup for the phase-contrast Fourier imaging. In what follows, subscripts p and t always denote the *probe* and *target* quantities, respectively. Both the target and probe laser beams are focused with different waists w_{0t} and w_{0p} with the incident beam diameters d_t and d_p , respectively. Both laser beams cross each other at their waists, where wave fronts are close to flat with $R = \infty$ in Eq. (8). We assume that the target waist w_{0t} is smaller than the probe waist w_{0p} , which embeds the phase contrast δ at z_0 within the amplitude on the transverse profile of the probe laser. The probe laser then propagates to a lens of focal length f_p and the inverse Fourier imaging is performed in the back focal plane of that lens.

We then define the geometry of the laser intersection. Figure 4 illustrates geometrical relations where the tightly focused target pulse with time duration τ_t , beam waist diameter $2w_{0t}$, and Rayleigh length z_{Rt} propagates along the Z -axis, and the probe pulse with the larger

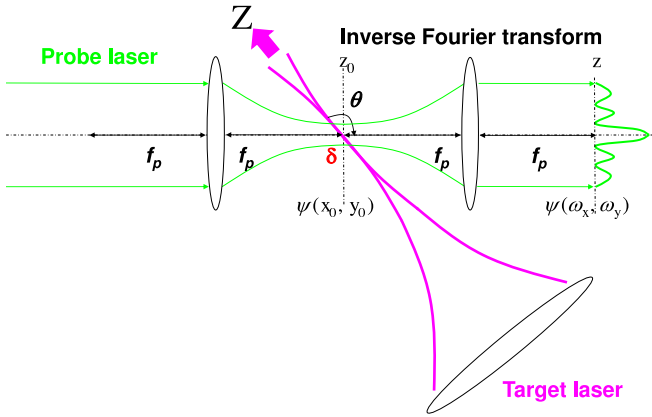


Fig. 3 Conceptual experimental setup for the suggested phase-contrast Fourier imaging. At the crossing point between the probe and target laser beams, the target pulse causes a shift in the index of refraction, and a corresponding phase shift δ embedded into the probe pulse as explained in Fig. 4.

beam waist diameter $2w_{0p}$ and longer time duration τ_p propagates along the z -axis tilted by θ with respect to the Z -axis. In Fig.4 a) and b) the pulses are assumed to have a rectangular intensity profile along the propagation direction. The dashed rectangular pulses occupy the positions at time $t = 0$ and the solid ones are those at $t = t_0$. The probe and target pulses overlap each other at the position marked by $*$. At this moment in time, t is taken as zero. We need to express δl to estimate the pass length where an additional phase is embedded. The path length δl is defined as the distance where the front of the probe pulse meets the edges of the target laser at $t = t_0$, beyond which the target laser is no longer present. In Fig.4 a) because A , B , and δl form a right triangle, we hence obtain the following relation

$$(\delta l)^2 = A^2 + B^2, \quad (15)$$

where $\delta l = ct_0$, $A = c(\tau_t - t_0)$ and $B = \tan(\pi - \theta)c(\tau_t - t_0)$ with the velocity of light c , resulting in

$$t_0 = \frac{\tau_t}{1 + \cos(\pi - \theta)}. \quad (16)$$

Depending on the relation between the target beam waist $2w_{0t}$ and the pulse length $c\tau_t$, namely, whether a) $A \leq 2w_{0t}$ or b) where the probe wavefront meets the side of the target laser before reaching the tail as shown in Fig.4, the optical path length δl is expressed as

a)

$$\delta l = ct_0 = \frac{c\tau_t}{1 - \cos\theta} \text{ for } c\tau_t < 2w_{0t} \frac{1 - \cos\theta}{\sin\theta}, \quad (17)$$

b)

$$\delta l = \frac{2w_{0t}}{\sin \theta} \text{ for } c\tau_t \geq 2w_{0t} \frac{1 - \cos \theta}{\sin \theta}, \quad (18)$$

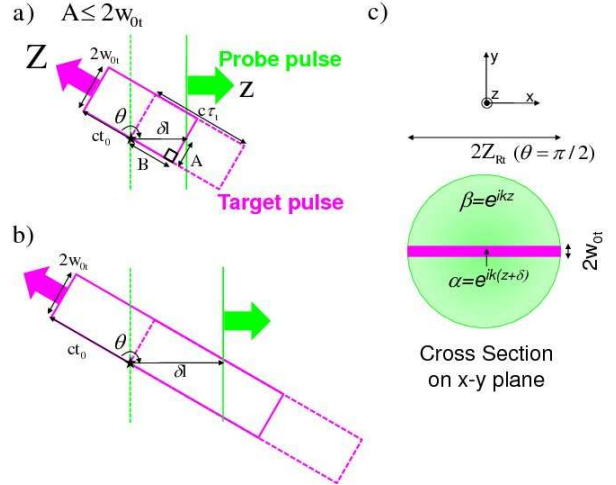


Fig. 4 Geometry of the embedded phase contrast in the probe pulse.

where the equations should not be applied to the cases $\theta = 0$ or $\vartheta = \pi$. In the case a) the path lengths with phase shift are not constant below or above the star point along the wavefront of the probe laser. In the case b) the path lengths are constant over the part of the probe wavefront which penetrates both sides of the target laser. The residual part along the wavefront, however, meets the head or tail of the target laser pulse and causes deviations from the constant path length. An exactly equal path length over the probe wavefront during the propagation time of the target laser $\sim 2z_{Rt}/c$ is realized only in the case of $\theta = \pi/2$. In this case, after the penetration of the probe laser pulse, the profile of the probe laser in the $x - y$ plane contains a trajectory with a constant phase shift δ along the projection of the path of the target laser on the probe wavefront, as shown in Fig. 4 c).

We express the phase shift δ in the vicinity of the waist $|z| = c\tau_t/2 \leq z_{Rt}$, where we assume that the wave-front is flat as indicated by Eq. (7) and Eq. (8)

$$\delta = \frac{2\pi}{\lambda_p} \delta n \delta l \varphi_t(x_p, y_p), \quad (19)$$

where δn is the refractive index shift, δl is the path length with an effectively constant phase shift over the crossing time and $\varphi_t(x_p, y_p)$ is a weighting function to reflect the path length difference depending on the incident position with respect to the target profile expressed as a function of the position (x_p, y_p) in the transverse plane of the probe laser. If we limit the origin of the laser-induced refractive index change to QED, based on Eq. (2), (3), and (4), we parametrize the refractive index shift as

$$\delta n_{qed} = \zeta N_0 (1 - \cos \theta) \frac{E_t}{\pi w_{0+} c \tau_t}, \quad (20)$$

where ζ is 4 or 7 for the polarization combinations \parallel or \perp , respectively. N_0 is the coefficient to convert from

energy density to the refractive index shift defined as $N_0 \equiv \frac{2}{45} \frac{\alpha^2 \hbar^3}{m_e^4 c^5} = 1.67 \times 10^{-12} [\mu\text{m}^3/\text{J}]$. The incident angle θ varies from 0 to π which is measured from the propagation direction of the target pulse to that of the probe pulse as depicted in Fig. 4. E_t is the energy of the target pulse given in [J], and $\pi w_{0t}^2 c \tau_t$ is the volume in $[\mu\text{m}^3]$ for the given target profile with the waist w_{0t} from Eq. (7).

By respecting the constant path length over $\sim 2z_{Rt}/c$ for simplicity, we consider only the case of (18) with $\theta = \pi/2$. By substituting Eq. (20) and (18) into Eq. (19), we obtain the simplest expression for δ_{qed}

$$\delta_{qed} \sim 4\zeta N_0 \frac{E_t}{\lambda_p w_{0t} c \tau_t}, \quad (21)$$

where $c \tau_t \geq 2w_{0t}$ must be satisfied from Eq.(18) and we take the approximation $\varphi_t(x_p, y_p) \sim 1$ to simplify the following argument (if necessary, we may restore the target profile $\varphi_t(x_p, y_p)$ based on the precise profile of the target laser reflecting actual experimental setups). In this limit we approximate the target profile as a rectangular of the size $2\mu \times 2\nu$, inside which the phase shift is assigned to be constant. The effective slit sizes are defined by the transverse sizes of the focused laser beams through the relation

$$\mu \sim z_{Rt} \text{ and } \nu \sim w_{0t}. \quad (22)$$

We then explicitly define the window functions rec and \overline{rec} as

$$rec(\mu, \nu) = \begin{cases} 1 & \text{for } |x| \leq \mu \text{ and } |y| \leq \nu \\ 0 & \text{for } |x| > \mu \text{ or } |y| > \nu \end{cases},$$

$$\overline{rec}(\mu, \nu) = \begin{cases} 0 & \text{for } |x| \leq \mu \text{ and } |y| \leq \nu \\ 1 & \text{for } |x| > \mu \text{ or } |y| > \nu \end{cases}. \quad (23)$$

This window provides a unit region of a constant phase, which may be applied even to arbitrary phase maps composed of a collection of the unit window cells.

We now discuss how the probe laser including the phase δ embedded at the focal plane propagates into the image plane via the lens system and evaluate the expected intensity distribution in the image plane. Since our discussion is based on local phases with rectangular shape and both Fourier and inverse Fourier transforms of a rectangular function give identical sinc functions, we represent the lens effect as Fourier transform. For each propagation from the object plane (x_0, y_0) at z_0 to the image plane (x, y) at z (see Fig.3), we always take the Fresnel diffraction. Based on (6) and (13), the probe field profile in the plane where the phase δ is embedded can be defined as

$$T(x_0, y_0) = A_p H_l \left(\frac{x_0}{\sqrt{2}\sigma} \right) H_m \left(\frac{y_0}{\sqrt{2}\sigma} \right) e^{-\frac{x_0^2 + y_0^2}{(2\sigma)^2}} \quad (24)$$

where $A_p \equiv \sqrt{\frac{I_0}{2\pi\sigma^2 2^{l+m} l! m!}}$ is the on-axis waist amplitude of the probe laser. The linearly synthesized amplitude at z_0 is then expressed as

$$\Psi(x_0, y_0, z_0) = \alpha(z_0) rec(\mu, \nu) T(x_0, y_0) +$$

$$\beta(z_0) \overline{rec}(\mu, \nu) T(x_0, y_0), \quad (25)$$

where $\alpha(z)$ and $\beta(z)$ are propagation factors of the probe waves at the point z after probe-target crossing. The functions α containing the phase shift δ caused by the local refractive index shift and β are defined as

$$\alpha(z) = e^{i(kz + \delta)},$$

$$\beta(z) = e^{ikz}. \quad (26)$$

The Fourier transform F of the synthesized amplitude Ψ in the image plane (x, y) at z after the lens [28] is expressed as

$$F\{\Psi(x_0, y_0)\} =$$

$$\alpha(z_0) F\{rec(\mu, \nu) T(x_0, y_0)\} + \beta(z_0) F\{\overline{rec}(\mu, \nu) T(x_0, y_0)\}$$

$$= (\alpha(z_0) - \beta(z_0)) \int_{-\mu}^{\mu} \int_{-\nu}^{\nu} dx_0 dy_0 T(x_0, y_0) e^{-i(\omega_x x_0 + \omega_y y_0)} +$$

$$\beta(z_0) \int_{-\infty}^{\infty} \int_{-\infty}^{\infty} dx_0 dy_0 T(x_0, y_0) e^{-i(\omega_x x_0 + \omega_y y_0)}, \quad (27)$$

where we define $(\omega_x, \omega_y) \equiv (\frac{2\pi}{f_p \lambda_p} x, \frac{2\pi}{f_p \lambda_p} y)$ at z . We introduce the coefficient C_s for the first term in Eq. (27), containing the information on how much the phase shift, representing the *signal*, is localized, resulting in the photon-photon interaction. We decompose C_s into its real and imaginary parts, because Hermite polynomials contain even and odd functions and the non-zero values of these integrals appear even in the imaginary part. We denote them as

$$\text{Re}C_s(\omega_x, \omega_y) \equiv C_{sR} =$$

$$\int_{-\mu}^{\mu} dx_0 \int_{-\nu}^{\nu} dy_0 \{ \cos(\omega_x x_0) \cos(\omega_y y_0) -$$

$$\sin(\omega_x x_0) \sin(\omega_y y_0) \} T(x_0, y_0)$$

and

$$\text{Im}C_s(\omega_x, \omega_y) \equiv C_{sI} =$$

$$- \int_{-\mu}^{\mu} dx_0 \int_{-\nu}^{\nu} dy_0 \{ \cos(\omega_x x_0) \sin(\omega_y y_0) +$$

$$\sin(\omega_x x_0) \cos(\omega_y y_0) \} T(x_0, y_0). \quad (28)$$

We also define the coefficient C_b for the second term of Eq. (27), which corresponds to the *background* pedestal as

$$C_b(\omega_x, \omega_y) \equiv$$

$$(-i)^{l+m} (2\sigma)^2 \pi H_l(\sqrt{2}\sigma \omega_x) H_m(\sqrt{2}\sigma \omega_y) e^{-\frac{\omega_x^2 + \omega_y^2}{(2\sigma)^2}}, \quad (29)$$

where the fact is used that the n_{th} -order Hermite function is the eigen-function of the Fourier transform, namely, $(2\pi)^{-1/2} F\{H_n(\xi) e^{-\xi^2/2}\} = (-i)^n H_n(\omega) e^{-\omega^2/2}$. We note that the coefficient $(2\pi)^{-1/2}$ arises due to our definition of the Fourier transform with the prefactor of

unity applied to the lens system. The Fourier transform of the amplitude is then expressed as

$$F\{\Psi\} = (\alpha - \beta)(C_{sR} + iC_{sI}) + \beta(C_{bR} + iC_{bI}). \quad (30)$$

When no confusions are expected, we will omit (x_0, y_0, z_0) and (ω_x, ω_y, z) for all relations below (30). By substituting Eq. (26), (28) and (29) into Eq. (30), the intensity pattern at the image plane is expressed as

$$|F\{\Psi\}|^2 = \psi_{l,m}\psi_{l,m}^* = \left(\frac{A_p}{f_p\lambda_p}\right)^2 \times \\ \{2(1 - \cos \delta)(C_s C_s^* - (C_{sR}C_{bR} + C_{sI}C_{bI})) \\ - 2 \sin \delta(C_{sI}C_{bR} - C_{sR}C_{bI}) + C_b C_b^*\}, \quad (31)$$

where $(f_p\lambda_p)^{-2}$ arises from the Fresnel diffraction. According to (29), when $l + m$ is even or odd, C_{bI} or C_{bR} becomes zero, respectively.

Equation (31) indicates that this method works as an interferometer via the cross terms with coefficients $1 - \cos \delta$ and $\sin \delta$. The second term with $\sin \delta$ vanishes for any combinations of l and m , as long as the symmetric rectangular ranges around $(x_0, y_0) = 0$ are assumed in the definitions of Eq.(28). This interferometer differs from a conventional one in that the modulating part due to the phase shift δ can be spatially separated from the confined strong part $C_b C_b^*$, due to the characteristic pattern of $C_s C_s^*$ which creates images in the region of higher spatial frequencies. In Eq.(31) the third term $C_b C_b^*$ corresponds to the intense pedestal pattern insensitive to the phase δ which keeps the same shape as that at z_0 with a different transverse scale based on Eq.(29), because Hermite functions are the eigen-functions of the Fourier transform. The second term shows proportionality to δ for $\delta \ll 1$; however, the intensity pattern is constrained by C_b . This implies the phase information is attainable only in the vicinity of the background pattern $C_b C_b^*$, though the signal is strong. Therefore, the signal-to-pedestal ratio is not expected to be large. On the other hand, the first term indicates proportionality to δ^2 for $\delta \ll 1$ which implies a very weak signal; however, the $C_s C_s^*$ term is not affected by C_b and it produces a pattern characterized by spatial frequencies. Hence the signal-to-pedestal ratio is expected to be drastically improved circumventing the most intense spot. Therefore, depending on the value of δ and the allowed dynamic range of the photo-detection device used, we have choices on which term we focus.

We consider a Gaussian beam with $l = m = 0$. Therefore, we do not expect the terms proportional to phase δ due to the imaginary parts originating from Hermite polynomials with odd orders. Nevertheless, if we need to stick to the proportionality to δ , we may add a local offset phase $\pi/2$ along the path of the target laser on the focal plane. We define this plane as the object plane for the inverse Fourier imaging as illustrated in Fig.5. Such a setup can recover the sensitivity to the sign of the phase shift as well as the absolute value, because

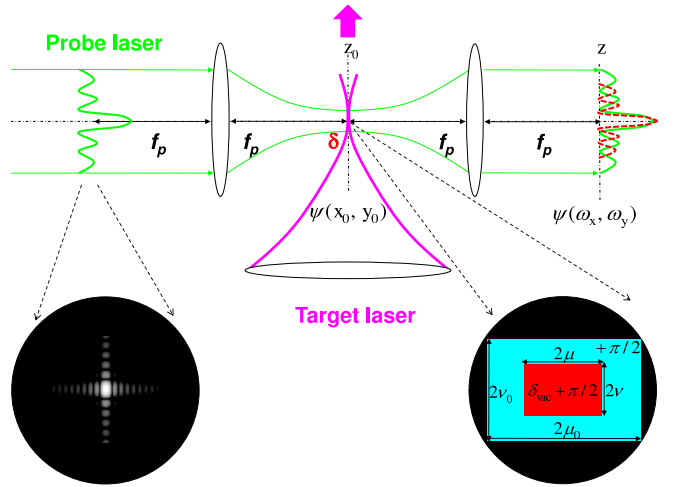


Fig. 5 Conceptual experimental setup for the suggested phase-contrast Fourier imaging. At the crossing point between the probe and target lasers, the target laser causes a shift in the index of refraction, which amounts to the refractive phase shift δ_{vac} embedded into the probe laser as explained in Fig. 4. The offset phase is embedded by a holographic phase plate in advance which provides the offset phase $+\pi/2$ inside the rectangular region $rec(\mu_0, \nu_0)$ at z_0 via Fourier transform by the first lens.

$1 - \cos(\delta + \pi/2)$ in Eq. (31) becomes $\sim 1 + \delta$. It is important to be able to discuss whether the phase shift is increased or decreased, since it directly reflects the dynamics of the local interaction. From a technical point of view, more importantly, this has a definite advantage of enhancing the signal due to the proportionality to δ compared to the δ^2 sensitivity in $1 - \cos \delta$ in case of an extremely small δ . However, in turn, one must accept the situation that the local offset phase contrast produces an intrinsic diffraction pattern as a new kind of pedestal, which now has an equal diffraction pattern compared to the one caused by the photon-photon interaction. Thanks to the proportionality to δ , we can reduce the intensity of the probe laser pulse. On the other hand, the new pedestal pattern would occupy the dynamic range of the camera device. In order to reduce the amount of the pedestal intensity, we may add more intelligent characteristic offset patterns by mixing $\delta \equiv \delta_{vac} \pm \pi/2$ with the laser-induced vacuum phase shift δ_{vac} and the offset phase $\pm\pi/2$ so that the offset diffraction patterns can destructively interfere in some points in the image plane thus still keeping a high signal-to-pedestal ratio. Therefore, the implementation of such local offset phases on the probe laser in advance is a key design issue, depending on the dynamic range of the camera device.

As illustrated in the zoom of the object plane (focal plane common to both lenses) in Fig.5, we consider a rectangular phase offset so that it contains the region with phase $\delta_{vac} \pm \pi/2$ in its center, that is, we define the offset region as $rec(\mu_0, \nu_0)$ with $\mu_0 = N\mu$ and $\nu_0 = N\nu$ and $N \geq 1$ in Eq.(23) by giving the offset phase of $\pm\pi/2$.

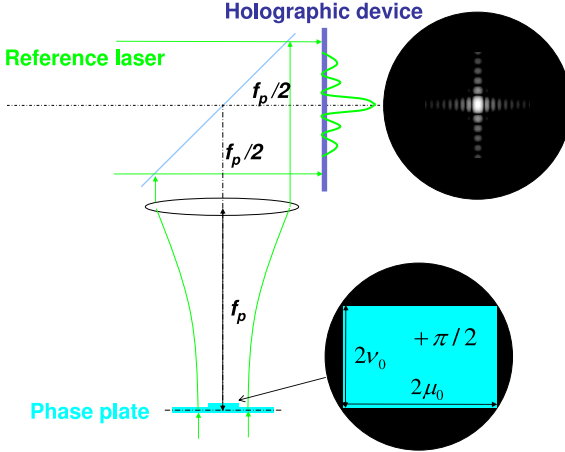


Fig. 6 An example how to implement the offset phase by a holographic device.

For this region we introduce the coefficient $C_0(\omega_x, \omega_y)$ by replacing (μ, ν) with (μ_0, ν_0) in Eq.(28) as well. The intensity profile in the focal plane is then re-expressed as

$$|F\{\Psi\}|^2 = \psi_{l,m} \psi_{l,m}^* \sim \left(\frac{A_{0p}}{f_p \lambda_p} \right)^2 \times \\ \{2(C_0 - C_b)(C_0 \pm \delta_{vac} C_s) + C_b C_b^*\}, \quad (32)$$

where \pm are cases when the offset phase $\pm\pi/2$ are added in $rec(\mu_0, \nu_0)$ and $\overline{rec}(\mu_0, \nu_0)$, respectively. We note that this relation is applicable to both real and imaginary coefficients as long as either all real or all imaginary coefficients are simultaneously zero. Actually we can confirm that Eq.(31) becomes identical with Eq.(32) under this condition, when $N = 1$ and $\delta_{vac} = 0$, namely, $C_s = C_0$ and $\delta = \pm\pi/2$ are substituted into Eq.(31).

The offset phase may be embedded by a sinc distribution which is, for example, produced via a step-like phase plate in advance via Fraunhofer diffraction by locating the plate at a far distance from the first lens in Fig.5. This may provide the offset phase $+\pi/2$ within the rectangular region $rec(\mu_0, \nu_0)$ at z_0 via Fourier transform by the first lens in Fig.5. If such a long distance is not available, we may use a holographic device as illustrated in Fig.6 where the phase plate is placed at the focal plane and a laser produces a proper Fourier image which is stored in the holographic device by mixing with a reference laser. If we replace the reference laser by the probe laser in Fig.5, we can produce the Fourier image in front of the first lens in Fig.5. In a practical case as shown in Fig.9, the holographic device may be located before the focal point when it records the local phases in advance, in order to supply an offset distance before the proper sinc distribution is reconstructed by probe laser pulses at the exact point where we need it.

3 Analysis in the Fourier image

We performed numerical calculations with the rectangular offset phase $+\pi/2$ based on the setup illustrated in Fig.5 with Eq.(32) for $l = m = 0$ (TEM_{00}). The parameters used for Fig. 7 are summarized in Tab. 1, where the parameters of the target and probe lasers, the embedded offset and the physical phase shifts due to the nonlinear QED effect used to obtain the Fourier transformed intensity distributions are specified. Figure 7 *top-left* illustrates the intensity pattern due to Eq.(32) as a function (x, y) in the image plane when $\delta_{vac} = 0$ and the offset phase $+\pi/2$ is embedded only. The figure is plotted with an arbitrary unit for the contour height in logarithmic scale, by sampling values with 5 mm steps along the x and y -axes. Figure 7 *top-right* shows the expected number of pedestal photons, N_{ped} integrated over a 1cm x 1cm cell along the y -axis at $x = 0$. Figure 7 *bottom-left* shows $N_{sig} - N_{ped}$ per 1cm x 1cm cell along the y -axis at $x = 0$, where N_{sig} is the integrated number of photons per 1cm x 1cm cell for signal, namely, with $\delta = \delta_{vac} + \pi/2$. In the actual experimental setup the subtraction should be performed on the shot-by-shot basis as illustrated in Fig.9 where a probe laser pulse is equally split into the signal path with the target laser pulse and the calibration path without it so that we can compare the two cases. The solid-red, dashed-blue and dotted-green histograms show the case when the probe wavelengths of 800nm, 840nm, and 760nm are assumed, respectively, and the yellow band shows the statistical fluctuations $\sqrt{N_{ped}}$ due to the quantum efficiency of the photon detection. Figure 7 *bottom-right* shows the statistical significance of the signal photons with respect to the statistical fluctuations of the pedestal photons; $(N_{sig} - N_{ped})/\sqrt{N_{ped}}$ per 1cm x 1cm cell along the y -axis at $x = 0$. The colors have the same meaning as those in Fig. 7 *bottom-left*.

Figure 7 *bottom-right* indicates that we can expect several cells in which the number of signal photons is either increased or decreased by more than two standard deviations from the pedestal fluctuations. If we could count the number of photons per 1cm x 1cm cell in the side band around the pedestal peak without detector saturation, we can measure the phase velocity shift due to the QED effect even by one probe-target laser crossing. This side band structure appears owing to interference between $C_0(\omega_x, \omega_y)$ and $C_s(\omega_x, \omega_y)$ in Eq.(32).

Although the spectral width of the probe laser shows faint effects as shown in Fig.7 *bottom-left* and *bottom-right*, the characteristic pattern along the y -axis is similar. As long as the wavelength distribution can be measured at the same time, we can reconstruct δ_{vac} based on the measured wavelength distribution and the intensity pattern along the y -axis.

The most difficult issue is the dynamic range of existing cameras used in research which typically have 16-bit resolution and at most 28-bit per pixel. In order to solve

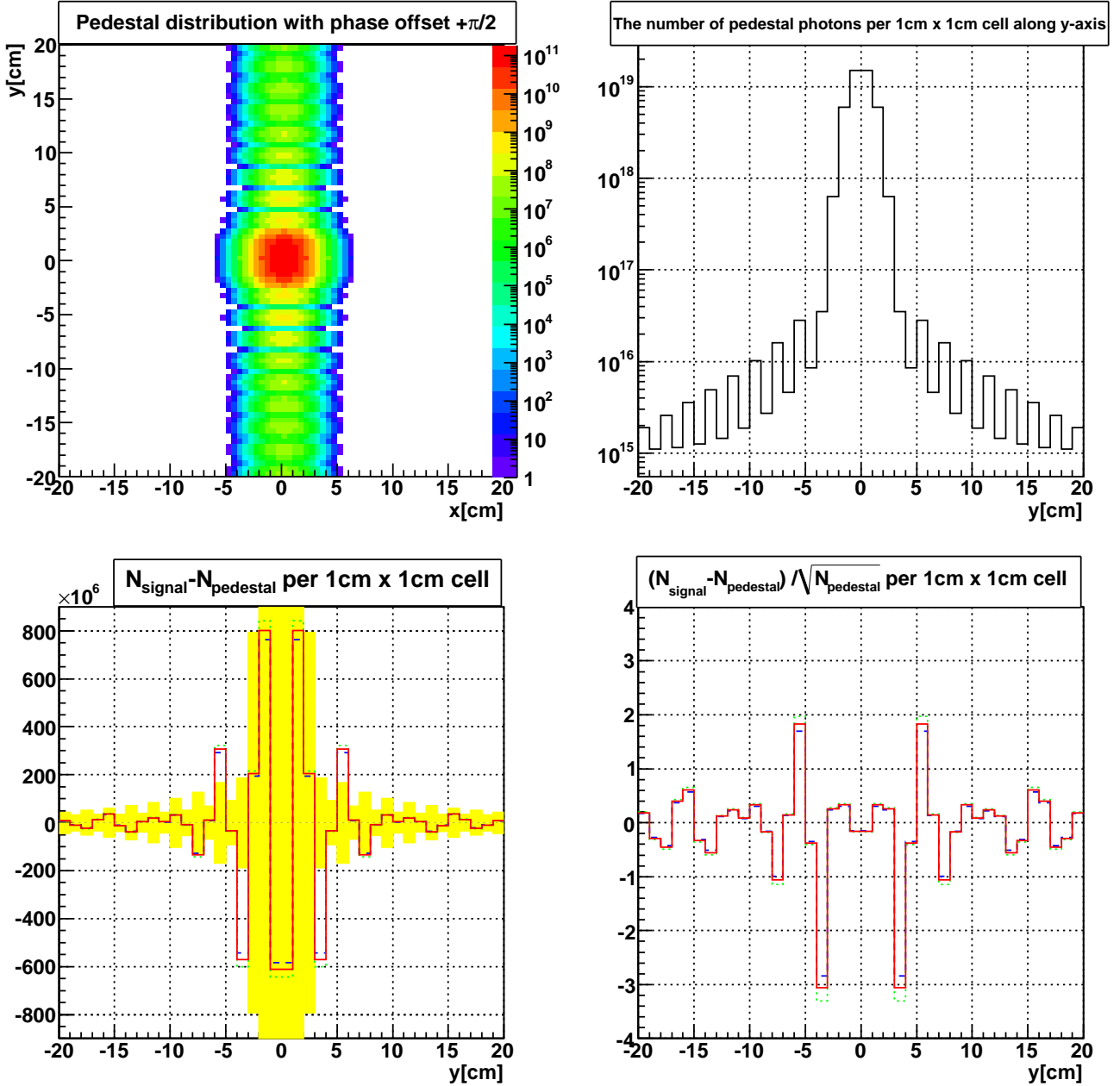


Fig. 7 Simulated distributions of $\psi_{0,0}\psi_{0,0}^*$ (TEM₀₀) in image plane z based on Eq.(32) with parameters given in Tab. 1. *top-left*: Patterns of Eq.(32) with the offset phase $+\pi/2$ only. *top-right*: The number of pedestal photons, N_{ped} integrated over a $1\text{cm} \times 1\text{cm}$ cell along the y -axis at $x = 0$ of the *top-left* distribution. *bottom-left*: $N_{\text{sig}} - N_{\text{ped}}$ per $1\text{cm} \times 1\text{cm}$ cell along the y -axis at $x = 0$, where N_{sig} is the integrated number of photons per $1\text{cm} \times 1\text{cm}$ cell with $\delta = \delta_{\text{vac}} + \pi/2$. The solid-red, dashed-blue, and dotted-green histograms in Fig.7 show the case when probe wavelengths of 800nm, 840nm, and 760nm are assumed, respectively, and the yellow band shows statistical fluctuations, $\sqrt{N_{\text{ped}}}$, due to the quantum efficiency of the photon detector. *bottom-right*: The statistical significance of signal photons with respect to the statistical fluctuations of the background photons; $(N_{\text{sig}} - N_{\text{ped}}) / \sqrt{N_{\text{ped}}}$ per $1\text{cm} \times 1\text{cm}$ cell along the y -axis at $x = 0$. The colors have the same meaning as those in the *bottom-left* chart.

Target laser parameters	Probe laser parameters
$\tau_t = 15$ fs	$\tau_p = 2z_{Rt}/c = 24$ fs
$E_t = 250$ J	$E_p = 25$ J
$\lambda_t = 800 \pm 40$ nm	$\lambda_p = 800 \pm 40$ nm
$d_t = 39.8$ cm	$d_p = 7.0$ cm
$f_t = 75$ cm	$f_p = 25$ cm
$w_{0t} \sim \frac{2f_t\lambda_t}{\pi d_t} = 0.96\mu\text{m}$	$w_{0p} \sim \frac{2f_p\lambda_p}{\pi d_p} = 1.8\mu\text{m}$
$z_{Rt} = \pi w_{0t}^2/\lambda_t = 3.6\mu\text{m}$	$z_{Rp} = \pi w_{0p}^2/\lambda_p = 18.5\mu\text{m}$
Embedded physical phase by assuming only QED effect	
$\delta_{qed} = 1.28 \times 10^{-10}$ from Eq.(21) with $\zeta = 4$ and $\theta = \pi/2$ in Eq.(20)	
Shape of physical and offset phases	
$\mu = z_{Rt}$ and $\nu = w_{0t}$	
$\mu_0 = 5 \times \mu$ and $\nu_0 = 5 \times \nu$ with offset phase $+\pi/2$	

Table 1 Laser parameters used to produce Fig. 7 based on the conceptual experimental setup shown Figs. 4 and 5. The subscripts t and p refer to the target and probe lasers, respectively. This choice of parameters is explained in the text in sections 2 and 3.

the limited dynamic range, let us suppose that we sample photons per $1\text{cm} \times 1\text{cm}$ cell by $\sim 10^6$ pixels. In such a case the number of photons per pixel is $\sim 10^9$ with respect to $\sim 10^{15}$ photons at around 5cm from the pedestal peak (see Fig.7 *top-right*). Even if we use 10-bit resolution, the number of photons per resolution becomes $10^9/2^{10} \sim 10^6$ photons. Compared to the $N_{sig} - N_{ped}$ of $\sim 10^8$ at around 5cm from the pedestal peak (see Fig.7 *bottom-left*), the sensitivity of 10^6 photons per resolution is sufficient to observe the intensity modulations beyond two standard deviations from the pedestal fluctuations without intensity saturation (see Fig.7 *bottom-right*). This suggests that in principle it is possible to detect the laser-induced QED effect by a single shot only if the conditions listed in Tab.1 are realized. Therefore, by assigning camera devices for individual $1\text{cm} \times 1\text{cm}$ cell with $\sim 10^6$ pixel readout, we can overcome the limited dynamic range of cameras even with the currently existing technology.

In order to study the laser-induced vacuum birefringence, we inject a linearly polarized probe pulse whose electric field vector is turned by 45 deg with respect to that of the target pulse so that its electric field along the x and y axes are equal. We then put two polarization filters at the image plane symmetrically with respect to $y = 0$ as illustrated in Fig.9 to cover the regions $+y$ and $-y$ along the y -axis, respectively, which select orthogonal polarizations at the image plane. The asymmetry between the number of modulated photons from that of the pedestal pattern between the regions $\pm y$ provides direct information of the birefringence on the pulse-by-pulse basis.

We note that this method bears similarity to that in [24], where two intense target laser pulses are treated as a matterless double slit and the interference between spherical waves from these slits is discussed as a signature of the photon-photon interaction. In [24] the occurrence of diffraction is caused by the laser-laser inter-

action itself. In our method the target laser causes the refractive phase shift experienced by the probe laser, as indicated in Fig. 5. This phase shift is embedded in a refracted, nearly-plane wave in the forward direction of the probe laser, as explicitly formulated in Eq. (25) and Eq. (26). We then set a lens to the right of the interaction between the target and probe lasers as shown in Fig. 5. The diffraction or Fourier transform in our method is incurred by the added phase of the lens and the spherical wave propagation from the lens to the focal plane. The advantage of our method is an enhanced sensitivity to a small phase shift on the pulse-by-pulse basis, as it is demonstrated due to a more efficient collection of photons by the lens using the much simpler target geometry. On the other hand, the disadvantage is the deviation from the ideal phases included in the path of the probe laser except the laser-induced vacuum phase. The ways to correct for this kind of background phase aberrations and the other background source for the phase-contrast Fourier imaging will be discussed in the following subsections.

3.1 Template analysis for local phase reconstruction

In actual experiments it is unavoidable that the probe pulse includes local phase fluctuations on a pulse-by-pulse basis even in the absence of the laser-induced signal δ as illustrated in Fig.8. The figure corresponds to the case when the phase contrast δ in Fig.5 c) is embedded in the presence of background phase fluctuations $\phi_i \equiv \phi(X)$ as a function of the position $X \equiv (x_0, y_0)$ at the object plane where i denotes a corresponding region with the constant phase ϕ_i in the transverse plane of the probe pulse. Compared to δ , the ϕ_i 's are expected to be much larger. However, if the values of the local phase set $\{\phi_i\}$ on each probe pulse is suppressed below the offset phase $\pi/2$ and the set is *a priori* measured, we are in principle able to correct for the effect of the background

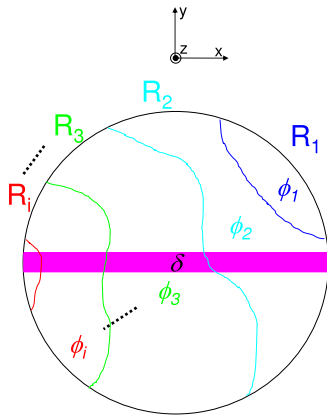


Fig. 8 The phase δ induced by the target laser pulse in the presence of local phase fluctuations in the transverse plane of the probe laser pulse at the object plane where the target and the probe pulses cross each other.

fluctuations. In the next subsection 3.2 we discuss how to measure the phase set on a pulse-by-pulse basis in detail. In this subsection, however, we focus on how to determine δ on a pulse-by-pulse basis, if the measured phase set is given in advance.

Let us extend the expressions from Eq. (23) through (27). In general, the integration limits defined by Eq. (23) and used in the first equation of (27) can take any shape and size. We replace the rectangular region rec with the region $R_i \equiv R(X)$, where a constant phase is mapped within R_i . By denoting the spatial frequency as $W = (\omega_x, \omega_y) = (2\pi x/(f_p \lambda_p), 2\pi y/(f_p \lambda_p))$, for the position (x, y) at the image plane with the integral kernel $f(W, X) \equiv T(x_0, y_0) e^{-i(\omega_x x_0 + \omega_y y_0)}$, the Fourier transform including the local phase fluctuations ϕ_i is expressed as

$$\begin{aligned} \Psi(W; \phi) &= F\{\Psi(X; \phi)\} \\ &= \sum_i^{N_X} \{\alpha(\phi_i) - \beta\} \int_{R_i} dX f(X, W) \\ &= \sum_i^{N_X} \{\alpha(\phi_i) - \beta\} \mathcal{F}_i(W) + \beta \mathcal{F}_\infty(W), \end{aligned} \quad (33)$$

where N_X is the number of regions in the transverse plane at z , $\alpha(\phi_i) = e^{i(kz + \phi_i)}$, $\beta = e^{ikz}$, $\mathcal{F}_i(W) = \int_{R_i} dX f(X, W)$, and $\mathcal{F}_\infty(W) = \int_{-\infty}^{\infty} dX f(X, W)$. We note that this expression corresponds to the regional cut and paste on $T(x_0, y_0)$; *i.e.*, cutting a region with a phase determined from β at z and paste the same region by adding ϕ_i in $\alpha(\phi_i)$.

Given ϕ_i on a pulse-by-pulse basis, we can numerically calculate the real and imaginary parts of $\Psi(W; \phi)$. The estimated background intensity pattern $I_{bg}(\phi)$ in the image plane with the phase fluctuations ϕ without

the laser-induced phase is given by

$$I_{bg}(W; \phi) = \{\text{Re}\Psi(W; \phi)\}^2 + \{\text{Im}\Psi(W; \phi)\}^2. \quad (34)$$

We now include as well a template of the laser-induced phase by the target laser pulse $\delta \equiv \delta(X)$. The phase shift δ can be evaluated from the geometry of the energy density profile of the target laser pulse. Based on Eq.(19) we parametrize δ as

$$\delta = \kappa \varphi_t(X), \quad (35)$$

where κ is a constant parameter that considers the absolute value of the phase shift induced by the target laser. The profile can be *a priori* determined by the experimental design of the focal spot. We can monitor if the center of the spot is in fact stable and further correct for its deviation from the fixed geometry of the target laser. Given δ , we only have to replace the phase by $\phi_i \rightarrow \phi_i + \delta$ with a constant parameter κ as follows

$$\begin{aligned} I_{bg+sig}(W; \phi + \kappa \varphi_t) = \\ \{\text{Re}\Psi(W; \phi + \kappa \varphi_t)\}^2 + \{\text{Im}\Psi(W; \phi + \kappa \varphi_t)\}^2, \end{aligned} \quad (36)$$

where *bg + sig* refers to the fact that the laser-induced phase is embedded in the background phase fluctuations.

Given the measured intensity pattern I_{meas} in the image plane per probe pulse, we define χ^2 with Eq. (36) as a function of κ

$$\begin{aligned} \chi^2(\kappa) \equiv \\ \frac{1}{N_W - 1} \sum_j^{N_W} \frac{|I_{meas}(W_j) - I_{bg+sig}(W_j; \phi + \kappa \varphi_t)|^2}{I_{meas}(W_j) + I_{bg+sig}(W_j; \phi + \kappa \varphi_t)}, \end{aligned} \quad (37)$$

where N_W is the number of sampling points in the image plane and j runs over all regions in this plane. The parameter κ can be determined by minimizing χ^2 on a pulse-by-pulse basis within the required accuracy.

3.2 Corrections on pulse-by-pulse phase aberrations

Figure 9 illustrates a schematic view of the entire system for the phase-contrast Fourier imaging including parts to correct all phase aberrations in the system. The target laser pulse moves perpendicular to the drawing plane. Its focus or waist lies in this plane. The signal path (SP) consists of the inverse Fourier transform part as discussed in Fig.5 and an array of mega-pixel camera sensors at the end to sample the intensity profile by individual 1cm x 1cm cells as discussed with Fig.7. In the SP the probe laser pulses are injected with the polarization tilted by 45 deg with respect to that of the target laser pulses. In front of the sensors, two polarizers (P) selecting photons with the orthogonal combination of polarizations so that the birefringence can be measured in a shot, which allows the statistical integration of the measurement over many shots by minimizing the systematic error due to shot-by-shot fluctuations

of the probe pulse energy. After the implementation of the holographic plate (HP) which produces the offset phase contrast in the laser interaction zone, we introduce a beam splitter (BS2) followed by the identical image transferring system as that in the SP. We refer to this leg as the calibration path (CP). We classify the origins of local phase fluctuations into the static component by the optical elements in the paths and the pulse-by-pulse component such as wavefront fluctuations included in the probe pulse coming from the upstream laser system. Since the repetition rate of the target laser is limited, we may inject a single-mode CW laser with the same wavelength as the dominant part of the probe pulse spectrum into both the SP and the CP, while the target laser pulses are not injected (Wavefront aberrations resulting from reflection by *BS1* are predetermined). Because a weak CW laser may be realized as a perfect Gaussian beam running in the TEM_{00} mode at a single longitudinal mode, we expect to be able to accurately determine the static phase component as the average value by using huge photon statistics accumulated over a long time period for an experiment while probe pulses are not injected. For the pulse-by-pulse component we use the intensity profile observed at the end of the CP to reconstruct a set of local phases caused by wavefront fluctuations included in the probe pulse on the pulse-by-pulse basis.

The measurable four types of local phase sets are denoted as ϕ_{SP}^{CW} , ϕ_{CP}^{CW} , ϕ_{SP}^{PLS} , and ϕ_{CP}^{PLS} where superscripts specify cases of CW and pulse laser injections, respectively, and subscripts refer to the different paths the beams take. In the following, all phase sets are interpreted as those defined on the focal plane, even if the local phases are actually embedded in different propagation points. The two phase sets in the SP are expressed by phases φ 's with subscripts corresponding to the names of the optical elements along the path in Fig.9 as follows:

$$\phi_{SP}^{CW} = \varphi_{HP} + \varphi_{BS2} + \varphi_{PM1_{SP}} + \varphi_{PM2_{SP}} + \varphi_{P_{SP}}, \quad (38)$$

and

$$\phi_{SP}^{PLS} = \varphi_{PLS} + \phi_{SP}^{CW}, \quad (39)$$

where *BS1* should be removed when the SP is active, and φ_{PLS} is the pure phase set caused by only the pulse-by-pulse component which is not correctable by the CW laser. The two phase sets in the CP are expressed as well

$$\phi_{CP}^{CW} = \varphi_{HP} + \varphi_{BS2} + \varphi_{PM1_{CP}} + \varphi_{PM2_{CP}} + \varphi_{P_{CP}}, \quad (40)$$

and

$$\phi_{CP}^{PLS} = \varphi_{PLS} + \phi_{CP}^{CW}. \quad (41)$$

Combining Eq.(39) and (41), we can restore the offset phase for the probe pulse injection in the SP, ϕ_{SP}^{PLS} by the other measured sets of phases as

$$\phi_{SP}^{PLS} = \phi_{CP}^{PLS} - \phi_{CP}^{CW} + \phi_{SP}^{CW}. \quad (42)$$

This implies that ϕ_{SP}^{PLS} can be restored by other measurable quantities, which is a necessary condition to allow the correction within the same probe pulse injection in the SP in the presence of the laser-induced vacuum phase shift. We finally describe the entire phase set in the focal plane in the SP when a target laser pulse exists as

$$\phi = \phi_{SP}^{PLS} + \delta_{vac}, \quad (43)$$

where $\delta_{vac} = \kappa\varphi_t$ as parametrized in Eq.(35). By substituting Eq.(43) into Eq.(37), we can, in principle, determine κ for the physical template based on the target laser profile φ_t .

The template analysis discussed in Sect. 3.1 can also be applied to determine the individual set of phases in the right hand side of Eq.(42). By assigning a square shape to the region R_i in Eq.(33), representing a cell instead of physical template φ_t in Eq. (37), we estimate κ_i for each $R_i(X)$. The number of photons at a point W_i in the image plane contains the convoluted phase information of the amplitude from all points in the transverse plane of the probe N_X as seen from Eq. (33). Therefore, as long as the number of sampling points in the image plane N_W is larger than that in the transverse probe profile N_X , we can, in principle, determine a phase set from Eq. (37) by scanning κ_i over the expected dynamic range of the phase variation. The achievable resolution of the phase reconstruction depends on the scanning step on κ_i in the χ^2 -test. As discussed with Fig.7 the phase-contrast Fourier imaging achieves at least the sensitivity of $\sim 10^{-10}$ for the physical phase shift by sampling the side band of the intensity distribution on the image plane. Therefore, we can introduce the same resolution step to determine κ_i . We may measure the initial coarse phase sets *a priori* by a commercially available wavefront sensor. From the phase measurement we can extract the set of phases at the focal plane by performing Fourier transform from the image plane back to the focal plane. Starting from this initial phase set at the focal plane, we perform the χ^2 -test to determine κ_i more accurately by comparing the computed Fourier image to the measured intensity at the image plane. If the resolution of commercially available wavefront sensors is limited to $\sim \lambda/100$, we would need to repeat the two-dimensional inverse Fourier transform from the focal plane to the image plane more than 10^8 times for scanning κ_i , in order to reach the same phase resolution as $\sim 10^{-10}$. Accordingly, a proper computing power is necessary to restore the sets of the offset phases in Eq.(42) on the pulse-by-pulse basis.

3.3 Background in the phase-contrast Fourier imaging

A background source of the current measurement is the refractive index shift due to the plasma creation from the residual gas along the path of the focused target laser pulse. The refractive index of the static plasma in the

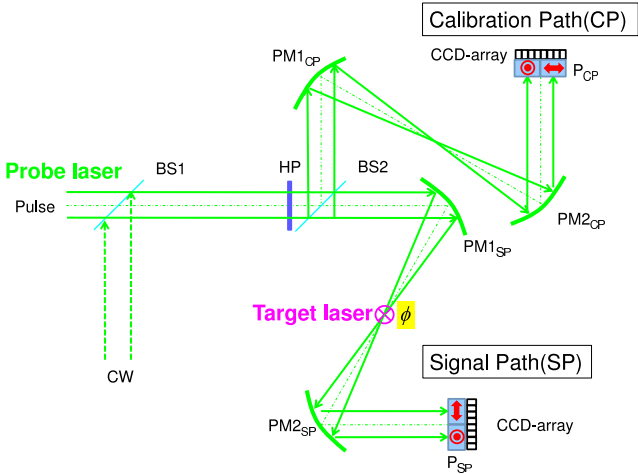


Fig. 9 Setup to correct local phase fluctuations.

limit of negligible collisions between charged particles is expressed as

$$N = \sqrt{1 - \frac{\omega_p^2}{\gamma\omega_0^2}}, \quad (44)$$

where ω_0 is the angular frequency of the target laser, ω_p is the plasma angular frequency defined as $\sqrt{4\pi e^2 n_e/m_e}$ and γ is the relativistic Lorentz factor given as $\sqrt{1 + a_0^2}$ with $a_0 = 0.85 \times 10^{-9} \lambda [\mu\text{m}] \sqrt{I_0 [\text{W/cm}^2]}$. In the low-pressure limit of the residual gas, the amount of refractive index shift $\Delta N \equiv N - 1$ is expressed as $\omega_p^2/2\gamma\omega_0^2$. Although the refractive index in the plasma becomes smaller than that of the peripheral area with neutral atoms, the inverted phase contrast of the phase shift inside the probe pulse still maintains a rectangular shape along the trajectory of the target laser. Therefore, it should produce the characteristic diffraction pattern at similar locations to the nonlinear QED case as expected from the Babinet's principle, which requires that the diffraction pattern from an opaque slit plus the inverted slit of the same size and shape form an amplitude distribution identical to that of the incident wave as we discussed in section 2. In order to reduce this effect, we need to reduce the electron density n_e in the residual gas. If we take $\gamma \sim 1$ as the upper limit of the ΔN estimate, the refractive index shift $\sim 10^{-11}$ due to the nonlinear QED effect for a reference energy density $\sim 1 \text{ J}/\mu\text{m}^3$, corresponding to a residual gas pressure of $\sim 10^{-5} \text{ Pa}$. The collisional frequency due to interactions between electrons and ions is expected to be $10^8 - 10^9 \text{ s}^{-1}$ at the critical electron density $n_{cr} [\text{cm}^{-3}] = 1.12 \times 10^{21} / \lambda^2 [\mu\text{m}]$, where ω_p equals ω_0 . For a duration time of $\sim \text{fs}$ of the target laser pulse, the inverse bremsstrahlung radiation due to collisional processes in the residual gas is negligible at $\sim 10^{-5} \text{ Pa}$.

Plasma formation is also caused by the probe pulse along its waist over a distance of $\sim 1 \text{ mm}$. At a pressure of $\sim 10^{-9} \text{ Pa}$ the associated plasma induced phase shift

is one order of magnitude smaller than that due to QED. Hence the pressure of the residual gas in the interaction chamber has to be kept at this level.

We note that the actual processes will be more dynamical, due to the ponderomotive force executed by the high-intensity laser field. In such a case the refractive index shift based on static plasma gives only the upper bound on the amount of the local refractive and phase shift.

4 Potential effects beyond QED

In the previous sections we discussed the design of the phase-contrast Fourier imaging by aiming at probing the vacuum birefringence through the QED effect, namely, the electron-positron loop to which photons couple. However, if the quark mass in vacuum is of the same order as the electron mass, we should expect that quarks also contribute to the vacuum birefringence by replacing the electron-positron loop with the quark-antiquark loop. Whether this effect has a sizable contribution or not is, however, difficult to quantify with presently existing field theoretical approaches, because of the strong coupling of quantum-chromodynamics (QCD) in vacuum, where the coupling is too large to allow for a perturbative treatment. Moreover, bare quark masses not confined in hadrons are not precisely known. In addition to calculations based on the QCD field theory [16, 17], there is another possibility that the duality between string theory with higher dimensions and field theory in 3+1 dimensions (holography) [18, 19] could be directly applicable to this birefringence problem [20]. The QCD and holographic approaches may give different predictions for the balance of coefficients between the two terms of the Euler-Heisenberg Lagrangian. Therefore, we may be able to pin down such theoretical issues by accumulating statistics more than a single shot and also expecting further increase of the laser intensity in the future.

Moreover, we note that because the photon-photon scattering cross section of QED interaction in the perturbative regime is so small, 10^{-42} b at optical frequency (see [29, 30]), we experience little 'noise', providing a pristine experimental environment to search for something beyond QED. Suppose then the detected dispersion and birefringence quantitatively deviate from the expectation of QED, including potential QCD corrections. This should indicate that undiscovered fields may be mediating photons beyond QED and QCD. Scalar and pseudoscalar types of fields in vacuum may contribute via the first and second products in the brackets of Eq. (1), respectively. They may be candidates of cold dark matter, if the coupling to photons and the mass are reasonably small [31]. Therefore, the measurement of the absolute value of the phase shift depending on the polarization combinations and the comparison to the expectations from nonlinear QED including potential QCD

corrections may be a general test of unknown nature in vacuum.

5 Conclusion

We suggest an approach to probe the vacuum birefringence under the influence of intense lasers. The phase-contrast Fourier imaging technique can provide a sensitive method to measure the absolute phase shift of light crossing intense laser fields. With this method nonlinear QED effects of the Euler-Heisenberg Lagrangian may be detected requiring no more than lasers of the hundred PW-class. The method provides a window for scoping the vacuum via the dynamics of the electron mass scale and possibly the lightest quark mass. Such a detection has never been made to date, and it heralds the research in the physics of the vacuum with a high-field approach. Given the high-intense optical lasers available in the ELI project [15] in the near future, the realization of this suggestion may become an exciting challenge for future experiments exploring vacuum physics.

Acknowledgment

This research has been supported by the DFG Cluster of Excellence MAP (Munich-Center for Advanced Photonics). K. Homma appreciates the support by the Grant-in-Aid for Scientific Research no.21654035 from MEXT of Japan. T. Tajima is Blaise Pascal Chair Laureate at the École Normale Supérieure. We thank H. Gies and S. Sakabe for their advices and P. Thirolf for his careful reading of our manuscript.

References

1. W. Heisenberg and H. Euler, *Consequences of Dirac's theory of positrons*, Z. Phys. **98**, 714 (1936) [arXiv:physics/0605038].
2. V. Weisskopf, Kong. Dans. Vid. Selsk. Math-fys. Medd. **XIV**, 166 (1936).
3. J. Schwinger, Phys. Rev. **82**, 664 (1951).
4. J.S. Toll, *The Dispersion Relation for Light and its Application to Problems Involving Electron Pairs*, dissertation, Princeton (1952).
5. N.B. Narozhnyi, Sov. Phys. JETP **28**, 371 (1969).
6. V. I. Ritus, Ann. Phys. **69**, 555 (1972).
7. W. Dittrich and H. Gies, *Probing the Quantum Vacuum*, Springer, Berlin (2000).
8. G.M. Shore, *Superluminality and UV completion*, Nucl. Phys. B **778**, 219 (2007) [arXiv:hep-th/0701185].
9. T. Heinzel and A. Ilderton, *Exploring high-intensity QED at ELI*, Eur. Phys. J. D **55**, 359 (2009) [arXiv:0811.1960 [hep-ph]].
10. G.V. Dunne, H. Gies and R. Schützhold, *Catalysis of Schwinger Vacuum Pair Production*, Phys. Rev. D **80**, 111301 (2009) [arXiv:0908.0948 [hep-ph]].
11. V.N. Baier and V.M. Katkov, *Pair creation by a photon in an electric field*, Phys. Lett. A **374**, 2201 (2010) [arXiv:0912.5250 [hep-ph]].
12. N. B. Narozhny, Zh. Eksp. Teor. Fiz. **54**, 676 (1968).
13. R. Schützhold, H. Gies and G. Dunne, *Dynamically assisted Schwinger mechanism*, Phys. Rev. Lett. **101**, 130404 (2008) [arXiv:0807.0754 [hep-th]]; N. B. Norozhny, Sov. Phys. JETP **27**, 360 (1968).
14. B. Marx, I. Uschmann, S. Höfer, R. Lötzsch, O. Werhrhan, E. Förster, M. Kaluza, T. Stöhlker, H. Gies, C. Detlefs, T. Roth, J. Härtwig, G.G. Paulus, *Determination of high-purity polarization state of X-rays*, Optics Communications **284**, 915-918 (2011).
15. <http://www.extreme-light-infrastructure.eu/>.
16. J. Rafelski and H.-T. Elze, *Electromagnetic fields in the QCD vacuum*, hep-ph/9806389.
17. H.-T. Elze, B. Müller, and J. Rafelski, *Interfering QCD/QED vacuum polarization*, hep-ph/9811372.
18. J. M. Maldacena, *The large N limit of superconformal field theories and supergravity*, Adv. Theor. Math. Phys. **2**, 231 (1998) [Int. J. Theor. Phys. **38**, 1113 (1999)] [arXiv:hep-th/9711200].
19. O. Aharony, S.S. Gubser, J.M. Maldacena, H. Ooguri and Y. Oz, *Large N field theories, string theory and gravity*, Phys. Rept. **323**, 183 (2000) [arXiv:hep-th/9905111].
20. A. V. Zayakin, *Properties of the Vacuum in Models for QCD: Holography vs. Resummed Field Theory: A Comparative Study*, PhD Thesis, LMU Munich (2010).
21. E. Zavattini, G. Zavattini, G. Ruoso, G. Raiteri, E. Polacco, E. Milotti, V. Lozza, M. Karuza, U. Gastaldi, G. Di Domenico, F. Della Valle, R. Cimino, S. Carusotto, G. Cantatore, M. Bregant, *New PVLAS results and limits on magnetically induced optical rotation and ellipticity in vacuum*, Phys. Rev. D **77**, 032006 (2008) [arXiv:0706.3419 [hep-ex]].
22. A.N. Luiten and J.C. Petersen, *Ultrafast resonant polarization interferometry*, Phys. Rev. A **70**, 033801 (2004).
23. A. Di Piazza, K.Z. Hatsagortsyan and C.H. Keitel, *Light diffraction by a strong standing electromagnetic wave*, Phys. Rev. Lett. **97**, 083603 (2006) [arXiv:hep-ph/0602039].
24. B. King, A. Di Piazza and C.H. Keitel, *Nature Photonics* **4** (2010), 92.
25. A.E. Siegman, *Lasers*, University Science Books, California, 1986.
26. For example, references are found in B. Quesnel and P. Mora, Phys. Rev. E **58**, 3719 (1998).
27. Amnon Yariv, *Optical Electronics in Modern Communications*, Oxford University Press, Inc., Oxford (1997).
28. Joseph W. Goodman, *Introduction to FOURIER OPTICS*, McGRAW-HILL CLASSIC TEXTBOOK REIS-SUE, McGraw-Hill, Inc. (1997).
29. R. Karplus and M. Neuman, Phys. Rev. **83** 776-784 (1950).
30. B. De Tollis, Nuovo Cimento **32** 757 (1964); B. De Tollis, Nuovo Cimento **35** 1182 (1965).
31. See section for *Axions and other similar particles* in C. Amsler et al. (Particle Data Group), Phy. Lett. B**667**, 1 (2008) and 2009 partial update for the 2010 edition.